Lab on a Chip

Accepted Manuscript

ROYAL SOCIETY OF CHEMISTRY

www.rsc.org/loc

Manuscript #LC-ART-04-2014-000476

Table of content entry

"We manipulate the splitting profile due to asymmetric forks to improve the enrichment of magnetic beads extracted from flowing droplets."

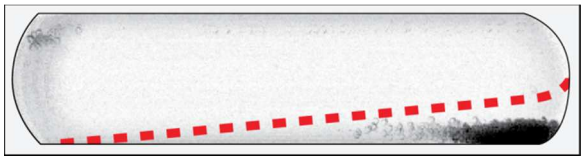

Journal Name

RSCPublishing

ARTICLE

Rapid and continuous magnetic separation in droplet microfluidic devices

Cite this: DOI: 10.1039/x0xx00000x

Eric Brouzes[a,*], Travis Kruse[a], Robert Kimmerling[a], Helmut H. Strey[a,*]

Received 00th January 2012,
Accepted 00th January 2012

DOI: 10.1039/x0xx00000x

www.rsc.org/

We present a droplet microfluidic method to extract molecules of interest from a droplet in a rapid and continuous fashion. We accomplish this by first marginalizing functionalized super-paramagnetic beads within the droplet using a magnetic field, and then splitting the droplet into one droplet containing the majority of magnetic beads and one droplet containing the minority fraction. We quantitatively analysed the factors which affect the efficiency of marginalization and droplet splitting to optimize the enrichment of magnetic beads. We first characterized the interplay between the droplet velocity and the strength of the magnetic field and its effect on marginalization. We found that marginalization is optimal at the midline of the magnet and that marginalization is a good predictor of bead enrichment through splitting at low to moderate droplet velocities. Finally, we focused our efforts on manipulating the splitting profile to improve the enrichment provided by asymmetric splitting. We designed asymmetric splitting forks that employ capillary effects to preferentially extract the bead-rich regions of the droplets. Our strategy represents a framework to optimize magnetic bead enrichment methods tailored to the requirements of specific droplet-based applications. We anticipate that our separation technology is well suited for applications in single-cell genomics and proteomics. In particular, our method could be used to separate mRNA bound to poly-dT functionalized magnetic microparticles from single cell lysates to prepare single-cell cDNA libraries.

Introduction

Droplet microfluidics permits the encapsulation of samples into low volume droplets which are immersed in an inert carrier oil fluid, and it also permits the high-throughput manipulation of these droplets in microfluidic channels to carry out basic operations required by biochemical workflows. Compared to conventional or other microfluidic methods, the droplet format confers many advantages: 1) contamination is prevented by the physical and chemical isolation of droplets from each other and from the surfaces of the devices; 2) droplets can be fully manipulated and easily retrieved at high throughput (up to 10 kHz) without any moving parts or elaborate automation; and 3) this technique is compatible with molecular biology techniques such as nucleic acid amplification by polymerase chain reaction (PCR) [1-4] or isothermal amplification [5]. In the past decade, droplet microfluidic technology has experienced tremendous growth [6, 7] and has been used to develop a wide range of applications such as: enzyme evolution [8, 9], drug screening [10], genetic analysis [4, 11], and single-cell and organism analysis [12-16]. These applications have been enabled mostly by the development of robust and high-throughput methods which allow controlled droplet generation [17-19], fusion [20, 21], injection [22], on-chip incubation [23, 24], sorting [25, 8], and splitting [26-34].

Unfortunately, it is difficult to adopt droplet microfluidics to more complex molecular biology workflows because it is lacking a robust method to enrich or extract target molecules. Such a method is important in situations where the target molecule is in a mixture that interferes with detection (e.g. background noise) or with biomolecular reactions (e.g. inhibition of desired enzymatic reactions). Our long-term goal is to develop an enrichment method for mRNA which is compatible and capable of performing single-cell RT-PCR. It is now well established that the cell lysate inhibits the RT step at high cell lysate concentration [35, 36]. Specifically, it has been shown in the context of microfluidics that the detection threshold for GADPH, a highly expressed gene, by RT-PCR is equivalent to 1 cell per 5 nL [37]. Some researchers addressed this problem by diluting the cell lysate through the addition of buffer to a droplet sub-volume obtained by splitting [38] or by using very large droplets [39]. In contrast, we have developed an approach based on the extraction of mRNAs bound to oligo-dT magnetic beads from droplets. In essence, we seek to adapt a macroscale method that has proven its utility in numerous

benchtop applications to a microfluidic format; and as such our method will have an impact beyond single-cell mRNA applications. Our approach consists in enriching mRNAs by marginalizing oligo-dT magnetic beads in a localized volume inside droplets, and specifically extracting that volume through droplet splitting using an asymmetric fork.

In this paper we perform a quantitative analysis and optimization of the factors which affect the enrichment efficiency. Our motivation is to study the effect of experimental parameters such as magnet strength and position, droplet velocity, and the design of the splitting fork on the enrichment of magnetic beads within microfluidic droplets. As we will illustrate, this system exhibits a complex coupling between internal flow fields and the forces acting on the magnetic particles. We optimized the extraction of bead-rich regions of droplets by designing asymmetric splitting forks that employ capillary effects to tailor the splitting profile. Our design is a major improvement over recent works [40, 41] which used a T-junction to split the droplets in half. Here, in one single pass, we are able to discard the majority of the cell lysate while retaining the complete collection of mRNAs, two factors that will contribute to quantitative single-cell RNA-Seq and the development of novel applications such as immunogenomics [42, 43]. By optimizing the microfluidics design of the splitting fork we created a robust, high efficiency, and rapid process, which shows significant improvements over existing methodologies, such as Electrowetting-on-dielectric (EWOD) droplet devices [44, 45].

Background

In this section we review the individual components of our separation technology.

Magnetic Interactions

The physics and applications of superparamagnetic beads in microfluidics have been reviewed extensively [46-48]. In this work, we used 1 µm diameter superparamagnetic microparticles (Dynabeads MyOne) whose magnetic properties are fully characterized [49]. They are commercially available in a variety of functional surfaces and can be used to purify mRNAs or proteins. Compared to larger magnetic microparticles (M-280 and M-450 with 2.8 and 4.4 µm diameter), the MyOne beads 1) have higher capacity per total weight because of their higher surface to volume ratio; 2) sediment much slower which allows to encapsulate the 1 µm bead solution into droplets without stirring; 3) are much less prone to clogging microchannels.

The magnetization of superparamagnetic microparticles at high fields is given by the following equation:

$$M = M_0 \left(1 - \frac{kT}{M_S \langle V \rangle B}\right) \quad (1)$$

where M_0 is the saturation magnetization, M_s the intrinsic spontaneous magnetization, kT the thermal energy, B the magnetic field, and <V> the mean volume of the magnetic nanocluster encapsulated in the bead. The saturation magnetization of MyOne beads is 23.5 Am^2/kg, resulting in an upper limit of the magnetic moment m for a single magnetic particle of $2.4x10^{-14}$ Am^2, with M_S=336kA/m, and $\langle V \rangle = 4.2x10^{-25} m^3$ (for more details see [49]).

To keep the design of the magnetic separation simple, we used rare earth Neodymium permanent magnets (K&J Magnetics) of Material type N42 and N52 with Residual Flux Densities of 1.31 T and 1.46 T respectively. We conducted magnetic field simulations using Maxwell 11.1 (Ansoft, PA) to estimate the fields and field gradients.

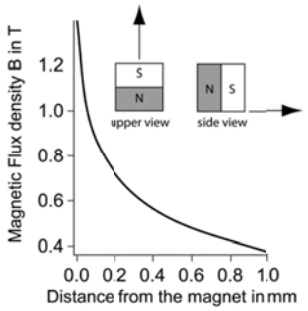

Fig.1: Magnetic field simulation using the finite-element method (Ansoft, PA). Plot shows how the B-field drops off as a function of distance measured away from the middle of one of the edges of a ¼'' x ¼'' x ¼'' N52 Magnet (insert).

The simulation results for a ¼'' cubic N52 magnet are shown in Fig.1. The magnitude of the B-field is plotted against the distance from the magnet along an axis which is perpendicular to and originates from the middle of the bottom side of the North Pole. At 200 µm the magnetic field is about 0.7 T and it decreases to 0.5 T at 600 µm. These values imply that the magnetic microparticles are almost fully magnetized ($m=2.3x10^{-14}$ Am^2 at 200 µm and $m=2.2x10^{-14}$ Am^2 at 600 µm) in our experimental conditions. Magnets are placed between 200 µm and 600 µm away from the channel and onto the glass slide used to make the microfluidic chips, their North-South axis is perpendicular to the straight channel used to flow droplets (Fig. 2).

Magnetic fields affect the behaviour of solutions of magnetic particles in two ways. First, the magnetic moments induced by the field result in inter-particle interactions and formation of chains oriented along the magnetic field lines. In our experimental conditions and values of flux densities and magnetic moments, the interaction energies at contact exceed thermal energies by many orders of magnitude. In fact, the magnetic flux density at which the contact energy is equal to thermal energy or kT is 50 µT (for a ¼'' cubic N52 magnet that corresponds to the magnetic flux at a distance of 10cm). Second, the gradient of the magnetic field exerts a force on the centre of mass of the magnetic beads [50] following the equation:

$$\vec{F} = \nabla(\vec{m}.\vec{B}) \quad (2)$$

In our case, the magnetic moment m is virtually saturated and therefore independent of B. Since the vectors $\vec{m}$ and $\vec{B}$ are parallel, we can simplify the expression for the force on a magnetic bead as follows:

$$\vec{F} = \nabla\left(\frac{m\vec{B}}{|\vec{B}|}.\vec{B}\right) = m\nabla|\vec{B}| \quad (3)$$

Using the same conditions as in Fig. 1, we estimated that the force due to the magnetic field gradient on a single microbead is about 50 pN at 200 µm and 20 pN at 600 µm. In our experimental conditions, gravitational forces are negligible compared to viscous, magnetic and capillary forces.

Flow fields inside droplets under plug flow

The main factor limiting the ability to separate particles inside a droplet plug are the interactions of the beads with the internal flow field which disperse beads and counteract the effect of the magnetic field. The hydrodynamics of droplet plugs has been reviewed recently [51] and we will summarize the main points here. Internal flow fields of droplet plugs strongly depend on the channel geometry. Plugs flowing in a cylindrical tube move slightly faster than the sheath liquid and therefore recirculating flows observed are similar to those in spherical droplets moving in the middle of a channel [52]. In rectangular channels the situation is reversed. In this case, droplets move slower than the sheath liquid, which passes by the droplets through the gutters at the four corners of the channel. This leads to internal flow fields, which follow the flow fields at the interfaces. The liquid is dragged toward the front of the droplet by the faster sheath liquid along the gutter, whereas the internal flow is directed backward next to the surfaces that are close to the channel walls [53, 54]. In the case of a train of droplets, counter-flows present in the gap between consecutive droplets can lead to stagnation zones in the flow field within the droplets and hydrodynamic interactions [34].

Coupling between magnetic and hydrodynamic forces

The distribution or dispersion of beads within droplets will depend on the interaction of assembled chains of magnetic beads with the flow field. Chains of magnetic particles exposed to rotating magnetic fields result in ensembles of rotating chains of average length [55]. As the frequency of the rotating magnetic field is increased the hydrodynamic friction forces overcome the dipolar magnetic forces and the chains break up. This behaviour applies to our system considering that a static magnetic field in a shear field should exhibit similar characteristics. As the magnetic chains grow longer the viscous forces acting on them in a uniform shear field get larger and ultimately will limit their size. Furthermore, the presence of these particles will also have an inherent effect on the flow fields. Therefore, we are faced with a complex coupling between all the interactions in this system. While this coupling needs to be understood to optimize the separation process, its detailed understanding is beyond the scope of this report which focuses on studying the effects of experimental parameters such as magnet strength, droplet velocity, and design of the splitting fork on the efficiency of the separation of magnetic beads within microfluidic droplets.

Design constraints for single-cell genomics

Since our goal is to capture the complete set of mRNAs from a single-cell lysate we first need to estimate the necessary number of magnetic beads per droplets. According to the manufacturer of our poly (dT) magnetic beads, each bead binds at least 2 fg of poly (A)+ mRNA. The amount of mRNA per cell is highly variable but can be as high as 0.5 pg in cultured cancer cells. We therefore estimate that we require at least 250 beads to capture all mRNAs. Since the encapsulation of beads is a statistical process (see also Supp. Fig. 2), we increased the number of beads to 350 per droplet to ensure that there are enough beads in each droplet to reliably bind all poly (A)+ mRNA.

As compared to previous works [40, 41], we significantly reduced the droplet size from several nanoliters to 0.2 nl in order to make the magnetic separation technique compatible with single-cell encapsulation approaches [56, 57]. The smaller volume also helps with reducing the time for mRNA binding to the beads.

Experimental

See supplemental information.

Results and Discussion

Encapsulating magnetic beads in the presence of a magnetic field

We first investigated the antagonistic effects of the magnetic field and the internal flows of droplets on the marginalization of magnetic beads. To do so, it is necessary to maintain the droplet size and the number of magnetic beads per droplet constant across the various experimental conditions. We first sought to encapsulate magnetic beads in the presence of a magnet, as previously described [40, 41], to simplify the experimental set-up. In the presence of a magnet located 16 mm away from the inlet, the magnetic beads form chains oriented along the magnetic field lines (Supp. Fig. 1a). Observation at the injection port reveals the presence of lateral magnetic interactions between these chains. The ensemble of magnetic beads exhibits a behaviour resembling granular media with the occurrence of dramatic events of bead release which result into an uneven flow of beads into the nozzle (Supp. Fig. 1b, Supp. Movie 1). The consequence of the presence of the magnetic field upon encapsulation is a large variation in the number of beads in different droplets (Supp. Fig. 1c). To further characterize the effect of the magnet on the encapsulation of the magnetic beads, we quantified the distribution of the number of beads across droplets as a function of droplet throughput, and compared those to the distribution of beads in the absence of a magnetic field (Supp. Fig. 1c). We can infer four different behaviours by comparing the distribution of magnetic beads in droplets to the case without magnet, with increasing throughput

we observe: I- much lower average number and much greater variation in the number of beads at low throughput; II- similar average number and variation for a narrow range of throughput; III- an increase of the variation in the number of beads across droplets; IV- a lower average number but a variation in the number of beads similar to the case without magnet. Our conclusion is that if we perform the encapsulation in the presence of a weak magnetic field we are unable to control and maintain a constancy of the number of beads between droplets. We thus adopted a strategy where we encapsulate magnetic beads and collect the droplets (Supp. Fig. 1d) in the absence of a magnetic field, and then re-injected them to study the marginalization of magnetic beads within the droplets as a function of magnetic strength and droplet velocity (Supp. Fig. 1e). This approach is made possible by the use of a fluorinated formulation which produces very stable emulsions. The scheme also permits to uncouple droplet size from the velocity which allow us to study the effect of a wide range of velocities on droplets of constant size. This approach also better reflects applications where cells are encapsulated and lyzed before mRNAs can be extracted. The average number of beads in droplets was 376 with a standard deviation of 24 throughout the experiments (Supp. Fig. 2).

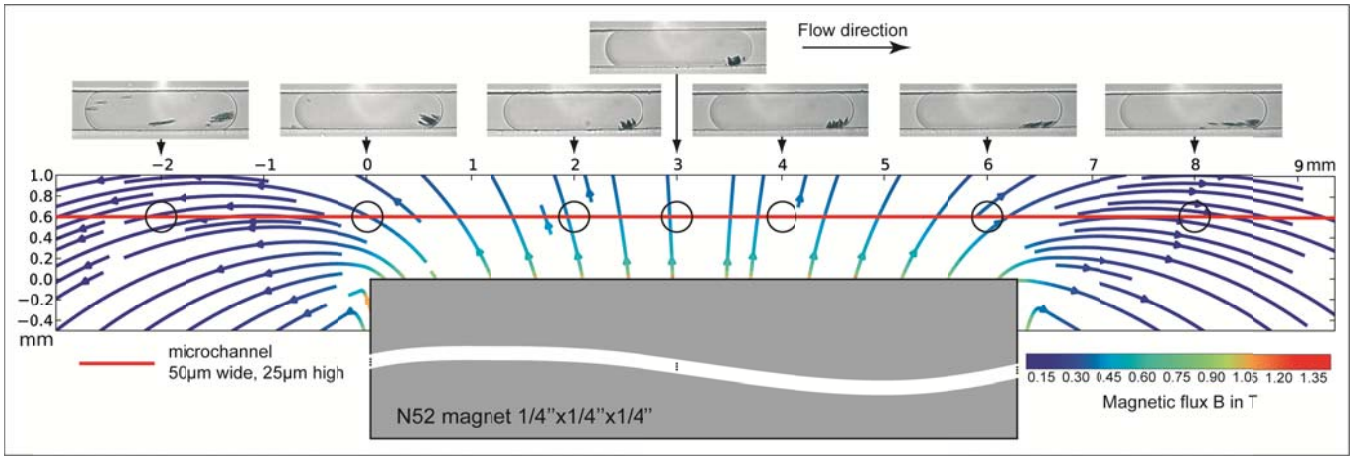

Fig. 2: Magnetic particle distribution and orientation as a function of position relative to the magnet. Particle aggregates are most compact when droplets reach the midsection of the magnet. Bead distribution is not mirror symmetric with respect to the magnet midsection because of internal flow fields. Microscopic pictures were taken at low velocity (0.8 mm/s) to approximate quasi-static conditions, with the N52 ¼" cubic magnet located at 635 µm from the channel.

Absence of marginalization of magnetic beads and flow pattern within droplets in the absence of magnetic field

Marginalization of particles can occur in plugs even in the absence of external field because of the presence of vortices and stagnation zones (or trapping mechanism) in the pattern of internal flows [58, 59]. We examined the distribution of beads inside droplets flowing at different velocities in absence of a magnetic field to check if the marginalization of magnetic beads was due to such effects. Under our experimental conditions and independently of the travel time of droplets inside the channel, magnetic beads are homogeneously distributed within the droplets (Supp. Fig. 3). At the scale of our experiments, the behaviour of magnetic beads is not affected by gravity which plays an essential role in the marginalization of larger glass microbeads (38 µm) inside plugs in the absence of other external field [59].

We then characterized the flow pattern inside those droplets in the absence of external field using high-speed videos and the magnetic beads as tracer particles (Supp. Movie 2). First, the average projection of the high-speed video frames exhibit a pattern which comprises four vortices-like structures but which cannot be resolved in the third dimension (Supp. Fig. 4a). Second, we extracted a qualitative flow pattern in the mid-plane of droplets by performing a Particle Image Velocimetry (PIV) analysis using the same video frames (Supp. Fig. 4b-5). The flow inside the droplets (in the frame of the droplet) appears to be made of a backwards plug-flow in the central region and lateral forward flows in narrow regions along the walls of the same velocity amplitudes on both sides, with vortices at the extremities to maintain flow continuity. This flow pattern is similar to those observed previously but for a higher viscosity ratio than water and HFE-7500 fluorinated oil [54]. It appears that the presence of numerous magnetic particles inside droplets increase the effective viscosity of the inner phase in this instance. In conclusion, there is a consistency between the flow pattern and the absence of marginalization of magnetic beads in the absence of an external field.

The distribution of magnetic beads depends on the position of droplets relative to the magnet

In order to optimize the extraction of magnetic beads from droplets we first identified the optimal position of the splitting fork. This question is equivalent to finding the position relative to the magnet which allows for the most concentrated distribution of beads within droplets. We re-injected droplets that contain magnetic beads past a permanent magnet at low velocity to approximate quasi-static conditions and neglect flow recirculation within droplets. Fig. 2 shows micrographs of droplets under these conditions as well as magnetic field lines and the magnitude of the magnetic flux as a function of position

relative to the magnet. The plane shown in the figure corresponds to the plane that supports the underside of the magnet and the microfluidic channel (see also Fig. 1).
Our data show that magnetic particles aggregate and collect towards the front and bottom of the droplet as the droplet flows past the magnet. This is consistent with the magnetic gradient forces acting on the magnetic bead aggregates. As shown in Supp. Fig. 6, there is a force which acts towards the magnet and there is a force which acts parallel and towards the middle of the magnet. At low flow rates, bead chains formed within droplets follow the orientation of the magnetic field lines. The aggregation of magnetic beads is more compact when droplets reach the midsection of the magnet where field lines are fully perpendicular to the channel. At this location, there is no force exerted on beads along the flow direction due to the gradient of magnetic field (Supp. Fig. 6). This pattern of bead aggregation along the channel remains true for higher velocities (data not shown). For these reasons, we conducted all our splitting experiments at this position.

The distribution of magnetic particles depends on droplet velocity and field strength

We further characterized the effect of the coupling of magnetic and hydrodynamic forces on particle distribution by quantifying the partitioning of magnetic particles within droplets. In Fig. 3, we report the fraction of beads located in the mid-section away from the magnet (top region) as a function of droplet velocity and magnetic strength which is modulated by varying the distance of the magnet to the channel. Magnetic forces are tabulated for a single MyOne bead using eq. 2, the values of the magnetic field are based on magnet properties (in this case, ¼" cubic N52 magnets), and the distance of the magnet to the channel (see Background section). Fig. 3 shows a contour plot of data for channel-magnet distances of 175 µm, 310 µm and 675 µm which correspond respectively to forces of 56 pN, 34 pN and 20 pN magnitude. Fig. 3 was created using python/numpy/scipy/matplotlib (www.scipy.org) by linear interpolating the experimental data as function of force and velocity. We performed the experiments with a train of droplets which were separated by 3-3.5 droplet lengths to avoid hydrodynamic coupling [34]. Droplet velocity was measured using a double exposure system. Data for each point represented by an open circle were compiled from a series of about one hundred images taken at the midsection of the magnet for each condition. To illustrate the local distribution of magnetic beads, we inserted pictures showing the minimal projection of these series of images.

Above a critical droplet velocity, which depends on the magnetic force, some beads start accumulating into the top back corner while most of the beads remain in the lower front corner. The higher the magnetic field strength the faster we can flow droplets to achieve the same bead distribution. However, the relationship between bead fraction in the top back corner and magnetic strength does not appear linear. There are minimal changes in the values of velocities which separate behaviours between 34 pN and 56 pN magnetic forces. However, there is a significant change in the values of velocities that characterize the boundaries of the separation behaviour between magnetic forces of 20 pN and 34 pN. Here, we are not reporting bead distribution at higher velocities because we are interested in cases where marginalization is favourable for biomolecular extraction.

It is difficult to provide a quantitative explanation for the behaviour observed. When beads are located within the span of the magnet, the force exerted on the center-of-mass of beads due to the gradient of magnetic field pulls beads toward the magnet in a direction parallel to the North-South axis (with a component in the third dimension not shown here) (Supp. Fig. 6). However, the analysis is complicated by the formation of bead chains and the description of the flow fields inside droplets. The internal flow fields depend strongly on the channel geometry and on the viscosity difference of the sheath and droplet liquids [54]. We could also expect that given the spacing between consecutive droplets there is no recirculating zones at the front and back of droplets [51]. In addition, the presence of bead aggregates is likely to influence the flow fields such that the latter will depend on the presence and the strength of the magnetic field [60]. We therefore focus on our engineering and experimental efforts to improve separation efficiency of magnetic beads inside droplets, and refer a more quantitative explanation for our observed distribution patterns to future efforts in flow simulations and hydrodynamic theory.

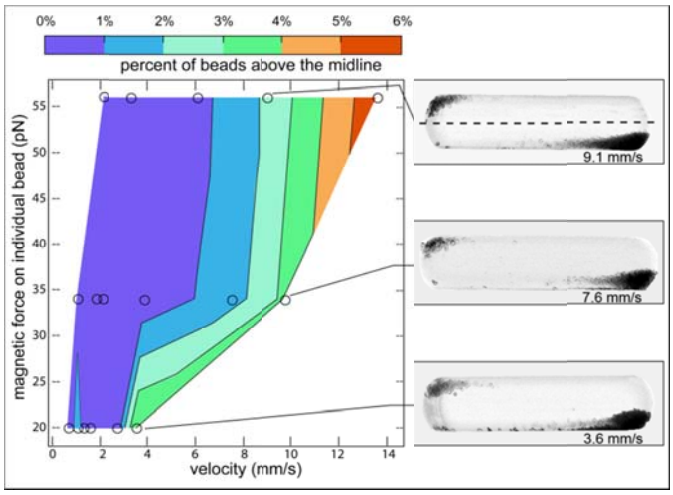

Fig. 3: Contour plot of the partitioning of magnetic particles plotted as percentage of magnetic beads above the midline (see top insert) as a function of droplet velocity and magnetic force. The circles represent the experimental points. The contour plot was created by linear interpolation in force and velocity. Inserts illustrate similar bead marginalization for different magnetic forces. Each image is the minimal projection of at least 45 individual droplets.

Splitting droplets for extracting magnetic beads

The second step of our strategy consists of physically splitting droplets to generate a pair of daughter droplets which respectively contain most of the magnetic beads and mostly buffer. This step will result into the formation of droplets containing enriched magnetic beads and attached analytes.

Droplet breakup or splitting has been discussed and studied extensively in the literature [26-34]. In summary, the critical parameter that controls the occurrence of droplet splitting is the capillary number which represents the relative effect of viscous forces versus surface tension acting on a system. The capillary number is defined as $C_a = \eta v / \gamma$, where η is the viscosity of the external phase, v the characteristic velocity and γ the oil-water interfacial tension. Since the interfacial tension drives the system to minimize the total interface, droplet breakup typically occurs above a threshold value of the capillary number. Here, we vary the capillary number by changing the droplet velocity, because we aim at improving the overall throughput of the separation and we keep the surface tension and viscosities of both phases constant.

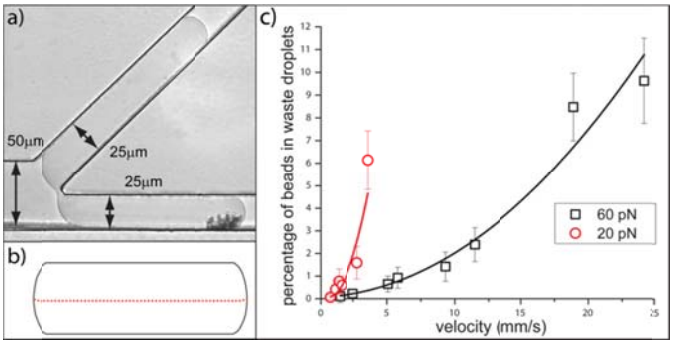

Fig. 4: Symmetrical splitting of droplets. a) Design and parameters of the splitting junction. b) We can infer the detailed splitting profile by analyzing the time-lapse sequences and measuring the projected surface areas of the two fronts in each channel (see Supp. Fig. 7). Splitting profile generated by the design confirms that droplets are split into two nearly identical daughter droplets. c) Separation efficiency measured by percentage of beads present in the distal daughter droplet as a function of droplet velocity and force exerted on a single magnetic bead by the permanent magnet (20 and 60 pN). The solid lines are least-square fits to a parabola to guide the eye.

We analysed the efficiency of separating and enriching magnetic beads with a 1:1 symmetrical split junction as a function of droplet velocity and magnetic force. We accomplished midline splitting by appending a fork made of two channels with the same dimensions and whose width is half the width of the main channel (25 µm and 50 µm respectively). This design assures that the hydraulic resistances of both branches are equal and that the splitting ratio is 1:1. Fig. 4a shows a droplet being split into two daughter droplets in an ideal case where all magnetic beads are segregated into the lower daughter droplet, this case results into a 2-fold enrichment of magnetic beads. We deduced the splitting profile by measuring the relative amount of droplet which enters the two channels during the splitting (Supp. Fig. 7). This method is useful to compare the splitting profile of different designs or at different velocities. The measured splitting profile confirms that the 1:1 symmetrical design produces identical daughter droplets (Fig. 4b).

In Fig. 4c, we reported the relative number of beads in the upper or "waste" droplet as a function of velocity and magnetic force. For both magnetic field strength conditions we fitted the data to a parabola to guide the eye. For low to moderate velocities the splitting efficiency follows the distribution from Fig. 3 which means that most particles aggregated in the lower front corner are separated into the lower droplets and that the beads present in the top back corner of the droplets are separated into the "waste" droplets. However, at higher velocities this correspondence is no longer true. This may be explained by the fact that the distribution of beads at the bottom front corner is not as tightly concentrated at higher velocities which results into the loss of some of those beads in "waste" droplets. We conclude that characterizing bead distribution in a droplet flowing past a magnet is a good predictor of separation efficiency at low to moderate velocities in the case of 1:1 midline splitting. In this configuration, the efficient separation of magnetic beads is mainly limited by the internal flow recirculation whose magnitude depends directly on droplet velocity and hence droplet throughput.

Harvesting capillary effects to tailor the splitting profile

In the previous configuration, the only option to improve separation efficiency would be to increase the magnetic force to counteract the dispersion of beads due to the internal flows of droplets. There is however another more subtle way to attain this goal if we consider that separation efficiency is a combination of minimizing the loss of magnetic beads and enriching beads in the split droplets. In other words, we can improve separation efficiency by minimizing the bead loss and by reducing the volume of the daughter droplet that retain them. This would result into a higher relative concentration of analyte-bound magnetic beads over the initial solution. The enrichment/purification factor obtained at each of the cycles would be higher, and the overall target factor would be attained with fewer cycles if the bead-containing droplets had a lower volume. In general, it would be preferable to accomplish the same final enrichment in fewer steps to reduce workflow complexity.

To minimize the volume of extracted droplets while maximizing bead retention, we developed a two-prong strategy to optimize the capture of the magnetic beads that accumulate in the lower front corner. It involves modulating both the splitting ratio and the splitting profile generated by the fork. The first component consists of changing the ratio of hydraulic resistances of the fork branches to create asymmetric splitting. It is expected that the volume ratio of the daughter droplet will directly reflect the ratio in hydraulic resistances [26, 27, 61]. It would result in sliding the horizontal splitting line as seen in Fig. 4b towards one channel wall. This approach is limited because beads form chains which can stretch up to the droplet midline. As a result, the more pronounced the splitting ratio the more likely beads at the lower front corner but close to the midline are lost.

The second component of our strategy employs design features to retain the lower front region while retaining less of the back of the droplet that is devoid of beads. It has been noted that in a certain regime of low to moderate capillary number, the volume ratio of daughter droplets does not follow the ratio of hydraulic resistance of the branches of an asymmetric design [32, 62, 34].

Instead, the hydraulic resistance ratio defines the plateau of volume ratio reached as the capillary number increases. We interpreted that this effect was due to capillary forces, and that the specific design of a splitting fork could have an important impact on the splitting profile in the low to moderate range of the capillary number. Indeed, at high capillary number (consider the extreme case where there is no interface) the flows split according to the ratio of hydraulic resistances, but in the range where capillary forces are not negligible there is an added effect of the Laplace pressure due to the droplet curvature. When droplets flow through a splitting fork the curvatures of the two fronts are dictated by the channel cross-sections in the case of non-wetting fluids. As a result, interfacial tension will tend to favour the larger cross-section because of the lower Laplace pressure to overcome. We sought to employ the effect of the capillary forces by changing the cross-section of the splitting channel: the first section of the splitting fork is similar to the symmetrical 1:1 fork, the channel cross-sections is then modified to provide a specific hydraulic resistance ratio (Fig. 5a). The intention is to first collect the front of the droplets at their midpoint and then decrease the amount collected from the back of droplets .

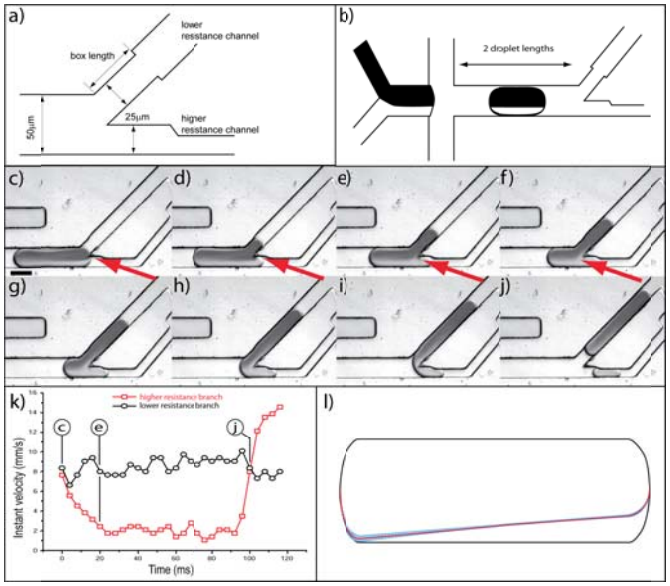

Fig.5: Tailoring the splitting profile. a) The design of the splitting fork consists of two branches of different hydraulic resistances where we incorporated an initial symmetrical box to favour the separation of the front lower region of droplets (here a 50 mm long box in front of a 1:3 splitting fork). b) We generated droplets with a 1:3 dark:light co-flow to emphasize the details of the splitting. The nozzle is located at 2 droplet lengths to avoid mixing inside the droplet and entrance effects. c) – j) depict the detailed splitting in a high-speed (500 fps) time-lapse series of a droplet flowing at 2.3 mm/s (2 ms between consecutive panels, 14 ms total sequence). The scale bar indicates 50 mm. c) the arrow indicates the initial location of splitting. d) the arrow points to some dark solution present in the lower branch, that later retracts into the upper branch (arrow in e). f) the arrow indicates the entry of the light solution into the upper branch. Gradually, more light solution follows the upper branch (g-i), until splitting. k) The analysis of the instant velocities of the two (lower and upper) fronts of the droplet indicates the presence of three phases during the splitting. Those phases are defined by the behavior of the droplet front in the higher resistance channel (lower branch), because the instant velocity of the droplet front in the lower resistance channel (upper branch) is constant. The first phase that lasts until the lower front reaches the end of the box is defined by a decrease of the instant velocity of the lower front (corresponding to the panels c-e). The velocity then reaches a constant value (panels e-j), until the droplet splits and the small droplet accelerates (panels j). l) We can infer the detailed splitting profile by analyzing the time-lapse sequences and measuring the projected surface areas of the two fronts in each channel (see Supp. Fig. 7). The panel depicts the splitting profile on the sequence c-j averaged over three droplets (the blue range indicates the standard deviation of the splitting profile).

To test our design hypothesis, we split droplets patterned with light and dark solutions in the ratio set by the ratio of hydraulic resistances of the channels in order to visualize the splitting profile. In the absence of capillary effects, the droplets should be split following the boundary between the light and dark solutions. We designed a microfluidic circuit that comprises a nozzle fed by a co-flow upstream of a splitting fork with a 50 µm long 1:1 box before a 1:3 hydraulic ratio couple of channels. The distance of the nozzle to the fork is equal to two droplet lengths to avoid both entry effects and mixing of the co-flow inside the droplets before the splitting (Fig. 5b). We conducted the experiment at a droplet velocity of 2.3 mm/s which is in the low range of the capillary number, and captured images with a high-speed camera at 500 frames per second (Fig. 5 c-j; Supp. Movie 3). Chronologically: the droplet hits the splitting fork at its midpoint; some dark solution enters the higher resistance channel; this dark solution later retracts into the lower resistance channel; the light solution starts flowing into the lower resistance channel when the droplet front in the high resistance reaches the end of the 1:1 box; the small droplet does not grow much until the droplet is split while the light solution keeps flowing into the low resistance channel. We confirmed the behaviour of the droplet during splitting by measuring the instant velocity of its two fronts (Fig. 5k). The instant velocities of both the droplet front in the lower resistance channel and of the droplet back (not shown) fluctuate around a mean velocity and can be considered constant during the splitting. On the contrary, the velocity of the droplet front in the higher resistance channel gradually decreases until it reaches a low constant velocity when the front reaches the end of the 1:1 box. Its instant velocity abruptly increases when the splitting is complete. We finally compared the amounts of the droplet which entered the low and high resistance channels between consecutive frames to extract the splitting profile generated by the design at this velocity (Fig. 5l). From these experiments, we can conclude that the channel restriction in the higher resistance channel acts as a capillary valve/diode [63, 64], and that the specific fork design is critical for the splitting profile at low capillary number. We can effectively employ capillary effects to tailor the splitting profile at low capillary number. From a practical point of view, it demonstrates that we can modulate the splitting profile in order to favour the extraction/enrichment of magnetic beads located in the lower front corner.

Optimizing the fork design

After validating our approach, we developed a rapid strategy to quickly identify a design that would improve upon the 1:1 fork design by measuring the splitting profile and the separation efficiency of 9 different designs at a droplet velocity of 5 mm/s which coincides to the regime where few beads are lost for the 1:1 splitting ratio with the stronger magnetic field (Fig. 4c). The designs are based on 3 split flow ratios of 1:3, 1:5 and 1:7, to which we appended a 1:1 ratio box of length 0 μm, 25 μm, and 50 μm.

The splitting profiles due to the different designs are reported in Fig. 6. In the absence of a 1:1 box the splitting profiles for the different split ratios remain flat and constant along the droplet length. As expected, increasing the hydraulic resistance ratio decreases the volume of the small daughter droplets. In contrast, inserting a 1:1 box at the tip of the splitting fork favours the extraction of the front region of the droplet by generating an inhomogeneous splitting profile. These data show that our strategy is valid for different split ratios and at a higher droplet velocity. The effect on the splitting profile is stronger with the 50 μm long box in all cases, as shown by the more pronounced slopes of their splitting profiles compared to the corresponding cases with the shorter 1:1 box. Finally, the design with a 1:3 hydraulic resistance ratio and a 50 μm long box offers the best magnetic bead extraction among the designs tested and a clear improvement upon the 1:1 fork design under these conditions (see Supp. Fig. 8 for typical data image of bead extraction for the whole series of designs).

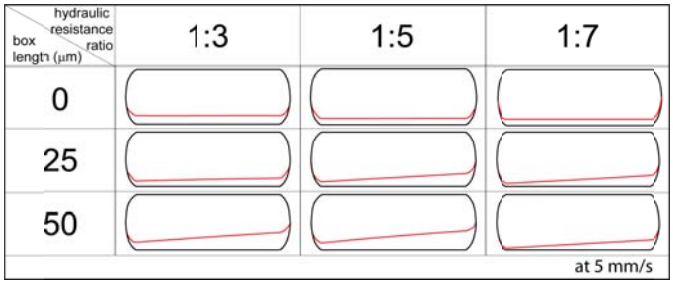

Fig. 6: Splitting profiles as a function of design. We tested the effect of different box designs on the splitting profiles of forks with different ratios of hydraulic resistances. We performed the experiments at 5 mm/s which is the velocity at which the performance of separation starts degrading for a 50:50 no box design (see Fig. 4c). The addition of a symmetrical box affects the splitting profiles of the different forks (only a representative splitting profile is shown for each velocity). Its effects permit to relatively collect more of the front versus the back of the droplets, which is devoid of magnetic beads in our case.

Characterizing the optimized design for magnetic bead extraction

We further characterized the separation efficiency of the 50 mm 1:1 box 1:3 split ratio fork design as a function of droplet velocity. In Fig. 7a we reported both the volume of bead containing droplets normalized by the initial volume of droplets, and the fraction of beads lost in "waste" droplets. We also superimposed the splitting profile on images that depict bead dispersion for each velocity.

As expected, droplet splitting occurs above a threshold in droplet velocity which is 2 mm/s in our experiments (Fig. 7a). Below this critical velocity we observed different behaviours when the capillary number (droplet velocity) increases (Supp. Movie 4): 1- where the droplets enter only the branch with the lower hydraulic resistance (not shown); 2- the droplets enter both branches but its front in the branch with the higher hydraulic resistance retracts and no splitting occurs; 3- and an additional case where splitting occurs but the smaller droplet remains blocked by the constriction that acts as a capillary valve/diode. These behaviours are similar to those already described [65, 31] with the additional case where the small droplet is blocked in the channel by the restriction (second scene in Supp. Movie 4). We did not seek to consistently map the different behaviours at low capillary number because this is not the regime of interest for our application.

The volume fraction of the extracted droplet increases with the capillary number until it reaches a plateau close to 0.27 that corresponds to the ratio of hydraulic resistances under operating conditions where interfacial tension can be neglected (or in the absence of an interface) (Fig. 7a). Our measured dependence of splitting ratio vs. velocity (or capillary number) is qualitatively similar to the ones previously reported where droplets are asymmetrically split by short or long obstacles that run parallel to the channels [32, 34]. However, expanding the previously proposed model to explain the dependency of droplet splitting ratio on capillary number [34] would necessitate to reflect the changes of channel cross-section, and hence capillary effects, experienced by droplets which flow through the box design.

The splitting profile also exhibits a dependence on the capillary number, while the point of splitting initiation remains essentially the same; the splitting profiles become more flat as the capillary number increases (Fig. 7b). At low capillary number, capillary effects dominate and the splitting profile is strongly affected compared to the case without the 1:1 box. As velocity is increased viscous effects counteract surface tension and start dominating the behaviour of the system. Overall, capillary effects modify the detailed splitting of droplets over a large range of droplet velocity validating our design approach. The splitting profile favours the extraction of the lower front region of droplets compared to the back of droplets for velocities up to 6 mm/s. We also reported the slope of the splitting profiles as a function of the capillary number (Fig. 7c), and we observed a scaling law between the slope and the capillary number. The range of experimental data would need to be extended to confirm the existence of this law. In conclusion, the experiments confirm and validate our hypothesis that we can employ capillary effects over a wide range of velocities in order to tailor the splitting profile of droplets.

The extraction data show that the amount of lost beads in the moderate velocity range (between 2 and 6 mm/s) is similar to those in the 1:1 split flow conditions (Fig. 7a, 4b); however, the enrichment of the extracted beads is two-fold higher, at 4-fold enrichment, because of the reduced volume of the extracted droplet. In this region the separation efficiency is limited only by the dispersion of beads into the quadrant diagonally opposite to the bead aggregation. The data

demonstrate the utility of the improved splitting profiles that permit to extract beads in the lower front corner despite a higher split ratio resulting into an improved enrichment. For higher droplet velocities, the number of beads in 'waste' droplets increases more dramatically in the 1:3 split flow condition. This demonstrates that the splitting profile at higher velocities is not pronounced enough to efficiently capture beads in the lower front region of droplets in those cases.

In theory, we should be able to expand the regime where capillary effects permit to modulate the splitting profile by improving the design of the splitting fork. This is the first report of measured splitting profiles of droplets, and we believe that more systematic studies and modelling would help in more fully understanding the parameters at work and in permitting to build a set of design rules to fine tune splitting profiles of droplets in different velocity ranges. Alternatively, we could also expand

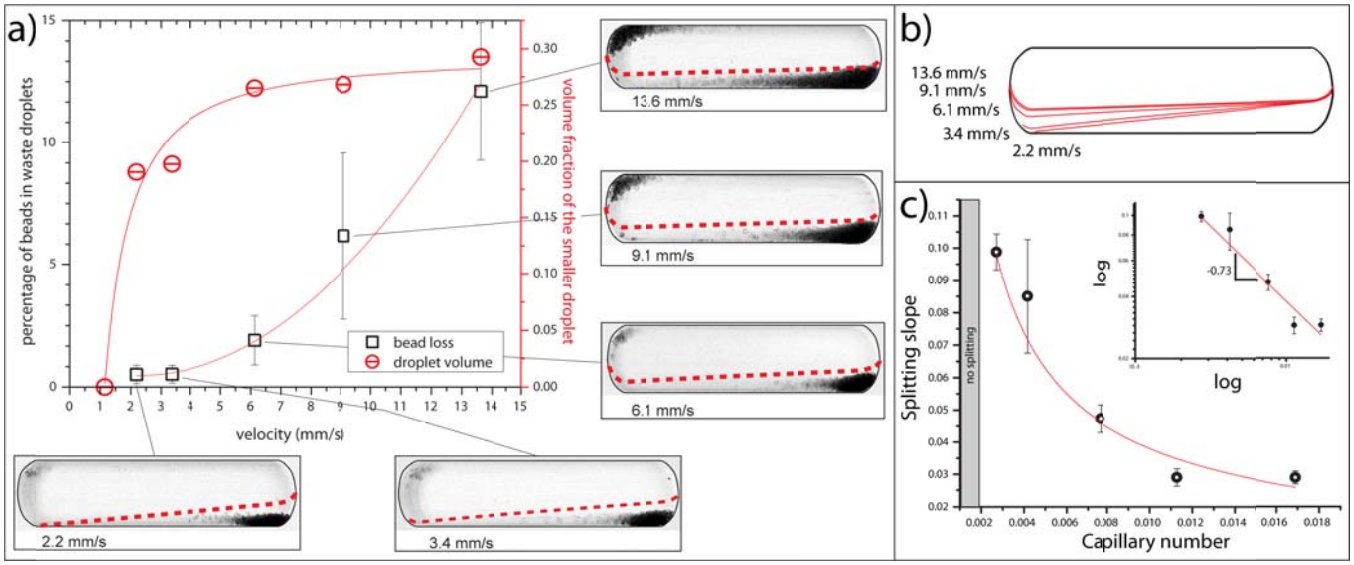

Fig. 7: Characterization of magnetic bead separation for the optimal splitting fork at 56 pN (1:3 resistance ratio and 50 mm long box, distance magnet to channel at 175 mm). a) The graph reports both the separation efficiency measured as the percentage of beads lost in waste droplets and the volume of the smaller droplet as a fraction of the initial droplet as a function of droplet velocity. Images depict the distribution of magnetic beads and the splitting profile for each velocity. b) Super-imposition of the different splitting profiles as a function of velocity (only a representative splitting profile is shown for each velocity). c) The plot of the splitting slope as a function of the capillary number indicates a relationship which tends to follow a power law with an exponent close to -3/4.

the velocity range where capillarity affects the splitting profile by using a droplet system with higher interfacial tension. For instance, the interfacial tension of a water and fluorinated oil containing 1% weight PEG-based surfactant has a value of 1 mN/m for the HFE7500 oil but a value of 20 mN/m for the FC-40 oil [66, 67].

The throughput of the magnetic bead separation at 98.1% retention of magnetic beads is about 15 droplets per second at 6 mm/s in the case where droplets are separated by two droplet lengths. The upper limit of throughput for droplet microfluidics is usually set by droplet generation, while we expect to perform droplet manipulations at one order of magnitude lower throughput. In our experimental conditions, the throughput of droplet generation is 1.5 kHz for 15 psi. The separation throughput is thus two orders of magnitude lower than the rate of droplet generation. This shows that the magnetic bead separation with good bead retention cannot yet reach the throughput of other droplet manipulations such as pair-wise merging [14]. On the other hand, the throughput of the overall workflow is determined by the enrichment ratio obtained for each cycle. One option for further improving the throughput is to run a series of separation modules stacked on top of each other to maintain similar magnetic forces and thus separation efficiency.

The optimal regime of separation will depend on the target application which determines the optimal balance between bead retention, throughput and total enrichment factor. For instance, the detection threshold of a highly expressed gene such as GADPH is 1 cell per 5 nL [37]. In our case, using 0.18 nL droplets we would need a 28-fold dilution which could be achieved with two 4-fold enrichment cycles followed by a 1:2 dilution during the addition of the RT-PCR reagents. In that situation the bead retention would not be as critical as for the detection of a low expressed gene, the throughput could be increased and the enrichment performed at 9 mm/s for an overall retention rate of $(0.85)^2$ or 72% for a 3.6-fold enrichment per cycle and 13-fold total enrichment. In contrast, for applications that seek to perform quantitative transcriptome analysis it would be beneficial to perform enrichment steps at lower velocity in the regime of higher bead retention and enrichment: the bead retention rates are 99.5% and 98.1% at 3.4 mm/s and 6.1 mm/s, for a 5-fold and 3.6 fold enrichment respectively.

For other enrichment applications it may be desirable to increase the droplet size. If we consider scaling the channel to maintain the droplet-slug aspect ratio, the shear forces which scale as the inverse of the typical cross-sectional length, are smaller for the same droplet velocity. As a result, the bead dispersion would be less pronounced. In addition, the number

of beads which depends on the quantity of target molecules, and hence the application, would remain the same and concentrate into a similar volume. That would allow the use of a greater splitting ratio and result into a larger enrichment factor per pass. However, the possibility of employing capillary effects to tailor the splitting profile may be altered because the capillary pressure scales as the inverse of the larger cross-section. Practical considerations, such as sample concentrations, reagent use, droplet stability and other more specific requirements (as in our case, see Background section) may place a lower bound on the droplet size. Finally, increasing droplet volume generally results in lower throughput droplet manipulations.

Conclusions

We have successfully demonstrated a method for rapid and continuous magnetic separation in droplet microfluidic devices. We have characterized the efficiency of marginalization of magnetic beads in droplets as well as the efficiency of splitting droplets as function of velocity and magnetic field strength. In addition, we designed and characterized novel splitting junctions that selectively capture the front bottom part of the droplet where the majority of magnetic beads are concentrated.

We have shown that our method can be customized to the needs of the specific molecular separation or enrichment application. Generally, we found that an increase in throughput or flow velocity will decrease both bead retention and enrichment ratio. Our novel splitting junction increases the enrichment ratio per pass but is limited to lower throughput because they rely on capillary effects. Our detailed characterization allows us to design custom separation chips with known bead retention and enrichment ratio per cycle.

We believe that our separation technology is well suited for applications in single-cell analysis. In particular, our method could be used to separate mRNA bound to poly-dT functionalized magnetic microparticles from single cell lysates to prepare single-cell cDNA libraries, or to capture cytokines released by single-cells.

Acknowledgements

We would like to thank Professor Cubaud (Stony Brook University) for helpful discussion and help with the high-speed camera. Research was carried out in part at the Center for Functional Nanomaterials, Brookhaven National Laboratory, which is supported by the U.S. Department of Energy, Office of Basic Energy Sciences, under Contract No. DE-AC02-98CH10886." This research was supported by funds from The Center for Biotechnology, an Empire State Development, Division of Science, Technology and Innovation (NYSTAR), Center for Advanced Technology, a grant from NIH-NHGRI (1 R21 HG006206-01), and a grant from NIH-NCI (R01 CA181595). EB received support from the Simons Foundation.

Notes and references

[a] Biomedical Engineering Department, Stony Brook University, Stony Brook, NY 11794-5281. * Corresponding authors.

Electronic Supplementary Information (ESI) available: Material and methods and Supplemental figures. See DOI: 10.1039/b000000x/

1. M. M. Kiss, L. Ortoleva-Donnelly, N. R. Beer, J. Warner, C. G. Bailey, B. W. Colston, J. M. Rothberg, D. R. Link and J. H. Leamon, *Analytical chemistry*, 2008, 80, 8975-8981.
2. Y. Schaerli, R. C. Wootton, T. Robinson, V. Stein, C. Dunsby, M. A. A. Neil, P. M. W. French, A. J. deMello, C. Abell and F. Hollfelder, *Analytical chemistry*, 2008, 81, 302-306.
3. N. M. Toriello, E. S. Douglas, N. Thaitrong, S. C. Hsiao, M. B. Francis, C. R. Bertozzi and R. A. Mathies, *Proc Natl Acad Sci U S A*, 2008, 105, 20173-20178.
4. R. Tewhey, J. B. Warner, M. Nakano, B. Libby, M. Medkova, P. H. David, S. K. Kotsopoulos, M. L. Samuels, J. B. Hutchison, J. W. Larson, E. J. Topol, M. P. Weiner, O. Harismendy, J. Olson, D. R. Link and K. A. Frazer, *Nature biotechnology*, 2010, 27, 1025-1031.
5. L. Mazutis, A. F. Araghi, O. J. Miller, J. C. Baret, L. Frenz, A. Janoshazi, V. Taly, B. J. Miller, J. B. Hutchison, D. Link, A. D. Griffiths and M. Ryckelynck, *Analytical chemistry*, 2009, 81, 4813-4821.
6. H. Song, D. L. Chen and R. F. Ismagilov, *Angewandte Chemie*, 2006, 45, 7336-7356.
7. A. B. Theberge, F. Courtois, Y. Schaerli, M. Fischlechner, C. Abell, F. Hollfelder and W. T. Huck, *Angewandte Chemie*, 2010, 49, 5846-5868.
8. J. J. Agresti, E. Antipov, A. R. Abate, K. Ahn, A. C. Rowat, J. C. Baret, M. Marquez, A. M. Klibanov, A. D. Griffiths and D. A. Weitz, *Proc Natl Acad Sci U S A*, 2010, 107, 4004-4009.
9. S. L. Sjostrom, Y. Bai, M. Huang, Z. Liu, J. Nielsen, H. N. Joensson and H. Andersson Svahn, *Lab Chip*, 2013, 14, 806-813.
10. O. J. Miller, A. El Harrak, T. Mangeat, J. C. Baret, L. Frenz, B. El Debs, E. Mayot, M. L. Samuels, E. K. Rooney, P. Dieu, M. Galvan, D. R. Link and A. D. Griffiths, *Proc Natl Acad Sci U S A*, 2012, 109, 378-383.
11. D. Pekin, Y. Skhiri, J. C. Baret, D. Le Corre, L. Mazutis, C. B. Salem, F. Millot, A. El Harrak, J. B. Hutchison, J. W. Larson, D. R. Link, P. Laurent-Puig, A. D. Griffiths and V. Taly, *Lab Chip*, 2011, 11, 2156-2166.
12. J. Clausell-Tormos, D. Lieber, J. C. Baret, A. El-Harrak, O. J. Miller, L. Frenz, J. Blouwolff, K. J. Humphry, S. Koster, H. Duan, C. Holtze, D. A. Weitz, A. D. Griffiths and C. A. Merten, *Chem Biol*, 2008, 15, 427-437.
13. S. Koster, F. E. Angile, H. Duan, J. J. Agresti, A. Wintner, C. Schmitz, A. C. Rowat, C. A. Merten, D. Pisignano, A. D. Griffiths and D. A. Weitz, *Lab Chip*, 2008, 8, 1110-1115.
14. E. Brouzes, M. Medkova, N. Savenelli, D. Marran, M. Twardowski, J. B. Hutchison, J. M. Rothberg, D. R. Link, N. Perrimon and M. L. Samuels, *Proc Natl Acad Sci U S A*, 2009, 106, 14195-14200.
15. Y. Zeng, R. Novak, J. Shuga, M. T. Smith and R. A. Mathies, *Analytical chemistry*, 2010, 82, 3183-3190.
16. T. Geng, R. Novak and R. A. Mathies, *Analytical chemistry*, 2014, 86, 703-712.
17. T. Thorsen, R. W. Roberts, F. H. Arnold and S. R. Quake, *Phys Rev Lett*, 2001, 86, 4163-4166.
18. S. L. Anna, N. Bontoux and H. A. Stone, *Applied Physics Letters*, 2003, 82, 364-366.
19. L. Frenz, J. Blouwolff, A. D. Griffiths and J. C. Baret, *Langmuir*, 2008, 24, 12073-12076.
20. K. Ahn, J. Agresti, H. Chong, M. Marquez and D. A. Weitz, *Applied Physics Letters*, 2006, 88, 264105.
21. L. Mazutis and A. D. Griffiths, *Lab Chip*, 2012, 12, 1800-1806.
22. A. R. Abate, T. Hung, P. Mary, J. J. Agresti and D. A. Weitz, *Proc Natl Acad Sci U S A*, 2010, 107, 19163-19166.
23. H. Song, M. R. Bringer, J. D. Tice, C. J. Gerdts and R. F. Ismagilov, *Appl Phys Lett*, 2003, 83, 4664-4666.

24. L. Frenz, K. Blank, E. Brouzes and A. D. Griffiths, *Lab on a Chip*, 2009, 9, 1344-1348.
25. K. Ahn, K. Kerbage, T. P. Hunt, W. R. M, D. R. Link and D. A. Weitz, *Applied Physics Letters*, 2006, 88, 024104.
26. D. R. Link, S. L. Anna, D. A. Weitz and H. A. Stone, *Phys Rev Lett*, 2004, 92, 054503.
27. Y. C. Tan, J. S. Fisher, A. I. Lee, V. Cristini and A. P. Lee, *Lab Chip*, 2004, 4, 292-298.
28. D. N. Adamson, D. Mustafi, J. X. Zhang, B. Zheng and R. F. Ismagilov, *Lab Chip*, 2006, 6, 1178-1186.
29. G. F. Christopher, J. Bergstein, N. B. End, M. Poon, C. Nguyen and S. L. Anna, *Lab Chip*, 2009, 9, 1102-1109.
30. T. Cubaud, *Physical Review E*, 2009, 80.
31. M.-C. Jullien, M.-J. Tsang Mui Ching, C. Cohen, L. Menetrier and P. Tabeling, *Physics of Fluids*, 2009, 21, 072001.
32. S. Protière, M. Z. Bazant, D. A. Weitz and H. A. Stone, *EPL (Europhysics Letters)*, 2010, 92, 54002.
33. A. M. Leshansky, S. Afkhami, M. C. Jullien and P. Tabeling, *Phys Rev Lett*, 2012, 108, 264502.
34. L. Salkin, A. Schmit, L. Courbin and P. Panizza, *Lab Chip*, 2013, 13, 3022-3032.
35. B. Arezi, M. McCarthy and H. Hogrefe, *Analytical biochemistry*, 2010, 400, 301-303.
36. J. Hedman and P. Radstrom, *Methods Mol Biol*, 2013, 943, 17-48.
37. A. K. White, M. VanInsberghe, O. I. Petriv, M. Hamidi, D. Sikorski, M. A. Marra, J. Piret, S. Aparicio and C. L. Hansen, *Proc Natl Acad Sci U S A*, 2011, 108, 13999-14004.
38. D. J. Eastburn, A. Sciambi and A. R. Abate, *Analytical chemistry*, 2013, 85, 8016-8021.
39. P. Mary, L. Dauphinot, N. Bois, M. C. Potier, V. Studer and P. Tabeling, *Biomicrofluidics*, 2011, 5, 24109.
40. D. Lombardi and P. Dittrich, *Analytical and Bioanalytical Chemistry*, 2011, 399, 347-352.
41. H. Lee, L. Xu, B. Ahn, K. Lee and K. Oh, *Microfluidics and Nanofluidics*, 2012, 13, 613-623.
42. B. J. DeKosky, G. C. Ippolito, R. P. Deschner, J. J. Lavinder, Y. Wine, B. M. Rawlings, N. Varadarajan, C. Giesecke, T. Dorner, S. F. Andrews, P. C. Wilson, S. P. Hunicke-Smith, C. G. Willson, A. D. Ellington and G. Georgiou, *Nature biotechnology*, 2013, 31, 166-169.
43. G. Georgiou, G. C. Ippolito, J. Beausang, C. E. Busse, H. Wardemann and S. R. Quake, *Nature biotechnology*, 2014, 32, 158-168.
44. Y. Wang, Y. Zhao and S. K. Cho, *Journal of Micromechanics and Microengineering*, 2007, 17, 2148-2156.
45. G. J. Shah and C. J. Kim, *J. Microelectromech. Syst.*, 2009, 18, 363-375.
46. M. A. M. Gijs, *Microfluidics and Nanofluidics*, 2004, 1, 22-40.
47. N. Pamme, *Lab Chip*, 2006, 6, 24-38.
48. M. A. Gijs, F. Lacharme and U. Lehmann, *Chem Rev*, 2010, 110, 1518-1563.
49. G. Fonnum, C. Johansson, A. Molteberg, S. Morup and E. Aksnes, *J Magn Magn Mater*, 2005, 293, 41-47.
50. S. S. Shevkoplyas, A. C. Siegel, R. M. Westervelt, M. G. Prentiss and G. M. Whitesides, *Lab Chip*, 2007, 7, 1294-1302.
51. C. N. Baroud, F. Gallaire and R. Dangla, *Lab Chip*, 2010, 10, 2032-2045.
52. Z. B. Stone and H. A. Stone, *Physics of Fluids*, 2005, 17, 063103.
53. H. Kinoshita, S. Kaneda, T. Fujii and M. Oshima, *Lab on a Chip*, 2007, 7, 338-346.
54. S. Ma, J. M. Sherwood, W. T. Huck and S. Balabani, *Lab Chip*, 2014, 14, 3611-3620.
55. S. Melle, O. G. Calderón, M. A. Rubio and G. G. Fuller, *Journal of Non-Newtonian Fluid Mechanics*, 2002, 102, 135-148.
56. M. Chabert and J. L. Viovy, *Proc Natl Acad Sci U S A*, 2008, 105, 3191-3196.
57. J. F. Edd, D. Di Carlo, K. J. Humphry, S. Koster, D. Irimia, D. A. Weitz and M. Toner, *Lab Chip*, 2008, 8, 1262-1264.
58. W. F. Fang, S. C. Ting, C. W. Hsu, Y. T. Chen and J. T. Yang, *Lab Chip*, 2012, 12, 923-931.
59. G. K. Kurup and A. S. Basu, *Biomicrofluidics*, 2012, 6, 22008-2200810.
60. B. Teste, A. Ali-Cherif, J. L. Viovy and L. Malaquin, *Lab Chip*, 2013, 13, 2344-2349.
61. M. Samie, A. Salari and M. B. Shafii, *Physical Review E*, 2013, 87, 053003.
62. A. Bedram and A. Moosavi, *The European physical journal. E, Soft matter*, 2011, 34, 78.
63. J. C. Eijkel and A. van den Berg, *Lab Chip*, 2006, 6, 1405-1408.
64. H. Boukellal, S. Selimovic, Y. Jia, G. Cristobal and S. Fraden, *Lab on a Chip*, 2009, 9, 331-338.
65. L. Ménétrier-Deremble and P. Tabeling, *Physical Review E*, 2006, 74.
66. R. Dangla, S. Lee and C. N. Baroud, *Physical Review Letters*, 2011, 107, 124501.
67. E. Brouzes, A. Carniol, T. Bakowski and H. H. Strey, *RSC Advances*, 2014, 4, 38542-38550.